This article was downloaded by: [FORTH]
On: 28 July 2015, At: 05:27
Publisher: Taylor & Francis
Informa Ltd Registered in England and Wales Registered Number: 1072954 Registered office: 5 Howick Place, London, SW1P 1WG

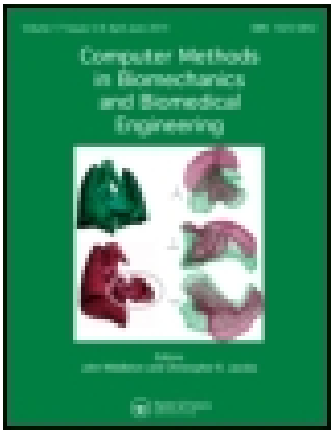

CrossMark
Click for updates

Computer Methods in Biomechanics and Biomedical Engineering
Publication details, including instructions for authors and subscription information:
http://www.tandfonline.com/loi/gcmb20

# A nonlinear dynamic finite element approach for simulating muscular hydrostats

V. Vavourakis[a], A. Kazakidi[a], D.P. Tsakiris[a] & J.A. Ekaterinaris[bc]

[a] Institute of Computer Science, Foundation for Research and Technology-Hellas, Heraklion, Crete 71110, Greece

[b] Department of Mechanical and Aerospace Engineering, University of Patras, Rio 26500, Greece

[c] Institute of Applied and Computational Mathematics, Foundation for Research and Technology-Hellas, Heraklion, Crete 71110, Greece

Published online: 01 Oct 2012.

To cite this article: V. Vavourakis, A. Kazakidi, D.P. Tsakiris & J.A. Ekaterinaris (2014) A nonlinear dynamic finite element approach for simulating muscular hydrostats, Computer Methods in Biomechanics and Biomedical Engineering, 17:8, 917-931, DOI: 10.1080/10255842.2012.723702

To link to this article: http://dx.doi.org/10.1080/10255842.2012.723702

PLEASE SCROLL DOWN FOR ARTICLE

Taylor & Francis makes every effort to ensure the accuracy of all the information (the "Content") contained in the publications on our platform. However, Taylor & Francis, our agents, and our licensors make no representations or warranties whatsoever as to the accuracy, completeness, or suitability for any purpose of the Content. Any opinions and views expressed in this publication are the opinions and views of the authors, and are not the views of or endorsed by Taylor & Francis. The accuracy of the Content should not be relied upon and should be independently verified with primary sources of information. Taylor and Francis shall not be liable for any losses, actions, claims, proceedings, demands, costs, expenses, damages, and other liabilities whatsoever or howsoever caused arising directly or indirectly in connection with, in relation to or arising out of the use of the Content.

This article may be used for research, teaching, and private study purposes. Any substantial or systematic reproduction, redistribution, reselling, loan, sub-licensing, systematic supply, or distribution in any form to anyone is expressly forbidden. Terms & Conditions of access and use can be found at http://www.tandfonline.com/page/terms-and-conditions

*Computer Methods in Biomechanics and Biomedical Engineering*, 2014
Vol. 17, No. 8, 917–931, http://dx.doi.org/10.1080/10255842.2012.723702

Taylor & Francis
Taylor & Francis Group

# A nonlinear dynamic finite element approach for simulating muscular hydrostats

V. Vavourakis[a1]*, A. Kazakidi[a], D.P. Tsakiris[a] and J.A. Ekaterinaris[b,c]

[a]*Institute of Computer Science, Foundation for Research and Technology-Hellas, Heraklion, Crete 71110, Greece;* [b]*Department of Mechanical and Aerospace Engineering, University of Patras, Rio 26500, Greece;* [c]*Institute of Applied and Computational Mathematics, Foundation for Research and Technology-Hellas, Heraklion, Crete 71110, Greece*

(*Received 12 January 2012; final version received 20 August 2012*)

An implicit nonlinear finite element model for simulating biological muscle mechanics is developed. The numerical method is suitable for dynamic simulations of three-dimensional, nonlinear, nearly incompressible, hyperelastic materials that undergo large deformations. These features characterise biological muscles, which consist of fibres and connective tissues. It can be assumed that the stress distribution inside the muscles is the superposition of stresses along the fibres and the connective tissues. The mechanical behaviour of the surrounding tissues is determined by adopting a Mooney–Rivlin constitutive model, while the mechanical description of fibres is considered to be the sum of active and passive stresses. Due to the nonlinear nature of the problem, evaluation of the Jacobian matrix is carried out in order to subsequently utilise the standard Newton–Raphson iterative procedure and to carry out time integration with an implicit scheme. The proposed methodology is implemented into our in-house, open source, finite element software, which is validated by comparing numerical results with experimental measurements and other numerical results. Finally, the numerical procedure is utilised to simulate primitive octopus arm manoeuvres, such as bending and reaching.

**Keywords:** FEM; large deformation; biological muscles; octopus

Downloaded by [FORTH] at 05:27 28 July 2015

## 1. Introduction

Muscles are often considered to be the bio-materials that, in contrast with other biological tissues, deform voluntarily. For this reason, simulation of muscle behaviour has been the subject of many research activities. However, due to muscles' complex mechanical nature (Fung 1993) and their ability to undergo large deformations, numerical simulation of such problems requires utilisation of a nonlinear approach. Finite element discretisation is the method of choice for the numerical solution of these problems.

Amongst the pioneering works in muscle mechanics, it was Beskos and Jenkins (1975) who proposed a theoretical model in order to describe the mechanical behaviour of mammalian tendon, in which the solid was assumed to be nonlinearly elastic or/and viscoelastic. However, among the first works in skeletal muscles' computational mechanics, Kojic et al. (1998) proposed a finite element method (FEM) for the determination of muscle response, where Hill's three-element model (Hill 1938) was used for the mechanical description of fibres. They accounted for the nonlinear force–displacement relation and change in geometrical shape; on the other hand, their major simplification was that the passive behaviour of the muscle is linearly elastic and isotropic, while no incompressibility was taken into account. Martins et al. (1998) developed a 3D finite element platform for the simulation of skeletal muscles, in which the constitutive relation adopted is a generalisation of the model proposed by Humphrey and Yin (1987), being compatible with the passive and active behaviour of skeletal muscles of Zajac (1989). Johansson et al. (2000) proposed a finite element approach for simulating the behaviour of muscles based on nonlinear continuum mechanics, where contractile active and passive properties of skeletal muscles were considered and incompressibility is fully incorporated. On the other hand, Oomens et al. (2003) proposed a finite element approach, in which physiological reasoning and 'cross-bridge' kinetics via a two-state Huxley model (Huxley 1957) was adopted for the investigation of mechanical behaviour of a tibialis anterior of a rat. Furthermore, Fernandez et al. (2005) presented a FEM muscle modelling framework that relates the mechanical response of the rectus femoris muscle to tissue level properties, with the capability of linking to the cellular level.

Recently, Liang et al. (2006), based upon the approach of Van Leeuwen and Kier (1997), have incorporated the governing equations for a muscle element into a commercial general-purpose explicit FEM programme. Their scheme is promising because it can simulate complex dynamic muscular behaviours but it suffers from the small time step restriction, required by numerical stability considerations. In the same year, Martins et al. (2006) introduced a multiplicative split of the fibre stretch into contractile and elastic stretches, where they considered the simultaneous presence of the series elastic element, the dependence of the

*Corresponding author. Email: vasvav@ucy.ac.cy

© 2012 Taylor & Francis

Downloaded by [FORTH] at 05:27 28 July 2015

contractile stress on the strain rate and an activation level function. Röhrle and Pullan (2007) also presented a 3D dynamic Galerkin FEM framework of an anatomically realistic model of the human masseter muscles and associated bones.

Further developments in muscle modelling were presented by Tang et al. (2007), in which Hill's muscle theory coupled with fatigue was proposed to describe the mechanical behaviour of skeletal muscles. They compared the proposed finite element technique with the experimental results on a frog muscle, capturing the real-time shape change due to fatigue. Stojanovic et al. (2007) proposed an extension of Hill's model of Kojic et al. (1998). They presented a model consisting of different types of sarcomere coupled in parallel with the connective tissues, in which each sarcomere was modelled by one nonlinear elastic element connected in series with one nonlinear contractile element. Tang et al. (2009) presented a 3D finite element model, developed to simulate the active and passive nonlinear mechanical behaviour of muscle during lengthening or shortening. The constitutive relation of the muscle was determined by using a strain energy approach, while the active contraction behaviour of the muscle fibre was modelled through Hill's three-element muscle concept. More recently, Lu et al. (2010) have developed a visco-hyperelastic model for skeletal muscles, in which the constitutive relation was based on the definition of a Helmholtz free energy function, involving 14 material parameters.

The literature survey demonstrates that the active muscle behaviour has been modelled with two main approaches: Hill-type- and Huxley-type-based models. However, in this study without loss of generality, it is assumed that the nominal tensile stress in muscles is derived from the maximum isometric stress, the normalised active level function, the velocity-dependent function, the filamentary overlap function and a passive component, similar to the approach of Van Leeuwen (1991). This rather simple approach is also referred to as the additive split of active and passive stresses, which is consistent with Hill's three-element model muscle representation of Van Leeuwen and Kier (1997).

This study was motivated by the OCTOPUS IP[2] project that aims to the design and development of octopus-like robotic arms. In connection to this objective, the development of a robust and efficient tool for the detailed study of the 3D kinematic and dynamic modelling of the octopus musculature is required. As it will be demonstrated in the numerical examples' section, this paper is a preliminary study on the biomechanical aspects (e.g. level and pattern of muscles activation) of the muscular hydrostats behaviour. To accomplish this, a first attempt to reproduce primitive octopus arm manoeuvres, such as arm bending and reaching, is made.

## 2. Numerical method

Consider a continuous, homogeneous, nonlinear, elastic medium of volume ${}^0V$ and surface ${}^0S$ in its unloaded state which undergoes large deformations. The volume and bounding surface of the body in its current (deformed) stated are denoted as ${}^tV$ and ${}^tS$, respectively.

A fundamental quantity for the description of deformation in nonlinear continuum mechanics (Holzapfel 2000) is the deformation gradient, which may be expressed in terms of the current coordinates ${}^tx_i$ of a material point or the displacements $u_i$ through the relation: $F_{ij} = \partial {}^tx_i/\partial {}^0x_j = \delta_{ij} + \partial u_i \partial {}^0x_j$, where $\delta_{ij}$ is the Kronecker delta. In addition, proper stress and strain measures are needed which relate these quantities with the currently deformed state of the solid body. Such measures are the Cauchy stresses $\sigma_{ij}$ and the left Cauchy–Green deformation tensor $B_{ij} = F_{ik}F_{jk}$.

Using quantities related to the current configuration, the equilibrium equations for a solid subject to finite deformation are nearly identical to those for small deformation analysis. The local equilibrium equation is obtained as a force balance on a small differential volume of the deformed solid

$$\frac{\partial \sigma_{ij}}{\partial {}^tx_j} = {}^t\rho \ddot{u}_i, \tag{1}$$

where body forces have been neglected and ${}^t\rho$ is the material density.

Proper boundary conditions are considered for posing the problem. Prescribed displacements are assumed on ${}^0S_{\mathrm{U}}$ and corresponding prescribed tractions are assumed on ${}^0S_{\mathrm{T}}$, with ${}^0S = {}^0S_{\mathrm{U}} \cup {}^0S_{\mathrm{T}}$.

In this study, muscles are assumed composite materials that comprise connective tissues and muscle fibres. Hence, it can be safely assumed that the stress distribution inside the element of the muscle is the superposition of stresses in the connective tissues and the fibres, i.e. $\sigma_{ij} = \sigma_{ij}^{(\mathrm{ct})} + \sigma_{ij}^{(\mathrm{f})}$, where the superscripts 'ct' and 'f' denote the connective tissue and fibrous part, respectively.

### 2.1 Connective tissues description

In most cases, biological tissues are best described through a hyperelastic Mooney–Rivlin (Mooney 1940) constitutive relation, in which the calculation of the Cauchy stress tensor can be obtained by differentiation of a stored energy function $W(I_1, I_2, J)$ with respect to deformation, where $I_1 = \mathrm{tr}(B_{ij})$, $I_2 = [I_1^2 - B_{kl}B_{lk}]/2$ and $J = \det(F_{ij})$.

However, rubber-like materials and biological tissues exhibit nearly or fully incompressible behaviour; thus, the $J \approx 1$ constraint must be satisfied. Towards this end, the following modified invariants are introduced: $\bar{I}_1 = I_1 J^{-2/3}$ and $\bar{I}_2 = I_2 J^{-4/3}$, based on the modified deformation gradient tensor $\bar{F}_{ij} = F_{ij} J^{-1/3}$ (Zienkiewicz and Taylor

Downloaded by [FORTH] at 05:27 28 July 2015

2005). Hence, the Cauchy stress tensor, in terms of $\bar{I}_1$, $\bar{I}_2$ and $J$, can be obtained by the following relation:

$$\sigma_{ij}^{(\mathrm{ct})} = \frac{2}{J^{5/3}}\left(\frac{\partial \bar{W}}{\partial \bar{I}_1} + \bar{I}_1 \frac{\partial \bar{W}}{\partial \bar{I}_2}\right) B_{ij} - \frac{2}{J^{7/3}} \frac{\partial \bar{W}}{\partial \bar{I}_2} B_{im} B_{mj} - \frac{2}{3J}\left(\bar{I}_1 \frac{\partial \bar{W}}{\partial \bar{I}_1} + 2\bar{I}_2 \frac{\partial \bar{W}}{\partial \bar{I}_2}\right)\delta_{ij} + \frac{\partial \bar{W}}{\partial J}\delta_{ij}. \tag{2}$$

By substituting the modified generalised Mooney–Rivlin constitutive material relation: $\bar{W} = c_1(\bar{I}_1 - 3) + c_2(\bar{I}_2 - 3) + K/2(J-1)^2$ into Equation (2), the analytic expression of the Cauchy stress tensor for the connective tissues is obtained:

$$\sigma_{ij}^{(\mathrm{ct})} = 2(c_1 + c_2\bar{I}_1)J^{-5/3}B_{ij} - 2c_2 J^{-7/3} B_{im}B_{mj} - \left[\left(\frac{2}{3J}\right)\!(c_1\bar{I}_1 + 2c_2\bar{I}_2) + K(1-J)\right]\delta_{ij}, \tag{3}$$

where $c_1$ and $c_2$ are the material constants and $K$ the bulk modulus, which for the present analysis assumes high values so that incompressibility is enforced via this penalty-like term.

### 2.2 Muscle fibres material description

The main structural components of the muscular system that plays on active role are the muscle fibres. Due to their contractive properties, the muscle contracts and causes muscle deformation. A muscle fibre comprises parallel bundles of myofibrils, which in turn are divided longitudinally by Z-discs into sarcomeres. However, a more detailed description of the muscular structure can be found in the work of Nigg and Herzog (1999).

Consider a uniquely defined direction vector at every material point of the muscle along the fibre, denoted with $\hat{n}_i$ and $\hat{m}_i$ at the reference (undeformed) and current (deformed) configuration, respectively. The updated fibre orientation is obtained by $\hat{m}_i = (F_{ij}\hat{n}_j)/\lambda$, where $\lambda = \sqrt{\hat{n}_i F_{ki} F_{kj} \hat{n}_j}$ is the fibre stretch ratio. The nominal strain is defined by the change in length divided by the reference length of the fibre and is given by $\varepsilon_0^m = \lambda - 1$. Therefore, the corresponding volume preserving fibre strain tensor can be written as (Liang et al. 2006): $\varepsilon_{ij}^{(\mathrm{f})} = \varepsilon_0^m(3\hat{m}_i\hat{m}_j - \delta_{ij})/2$, whereas the corresponding Cauchy stress tensor has the form

$$\sigma_{ij}^{(\mathrm{f})} = \sigma^m \hat{m}_i \hat{m}_j, \tag{4}$$

where the nominal axial stress $\sigma_0^m$ is defined in terms of the Cauchy true fibre stress: $\sigma^m = \sigma_0^m(\varepsilon_0^m + 1)$.

According to Van Leeuwen (1991), the fibre nominal axial stress in muscles is defined as the accumulation of passive $\sigma^{(\mathrm{pass})}$ and active axial stress. The latter part is considered to be the product of the maximum isometric stress $a^{(\max)}$ at fibre optimum length, a normalised active state function $f^{(a)}(t)$ that describes the activation pattern, a force–length $f^{(l)}$ and a force–velocity function $f^{(v)}$ that relate the active muscle stress with $\varepsilon_0^m$ and $\dot{\varepsilon}_0^m$, respectively. The above assumptions are based upon the sliding filament theory of Huxley (1957). Thus, the nominal axial stress in a muscle fibre can be expressed as below

$$\sigma_0^m = \sigma^{(\mathrm{pass})} + \sigma^{(\max)} f^{(a)} f^{(l)} f^{(v)}. \tag{5}$$

### 2.3 Finite element discretisation

The balance Equation (1) can be replaced by an equivalent principle of virtual work, which has to be in a form appropriate for finite deformations. The variational theorem for finite elasticity in the current configuration (Zienkiewicz and Taylor 2005) reads

$$\delta\Pi = \int_{{}^tV} \delta D_{ij}\sigma_{ij}\mathrm{d}V - \int_{{}^tS_{\mathrm{T}}} \delta v_i \bar{t}_i \mathrm{d}S + \int_{{}^tV} \delta v_i\, {}^t\rho \ddot{u}_i \mathrm{d}V = 0, \tag{6}$$

where ${}^t\rho$ is the current material density, $\bar{t}_i$ is the prescribed tractions on ${}^0S_{\mathrm{T}}$, $\delta v_i$ is an admissible velocity variation that satisfies the condition: $\delta v_i = 0$ on ${}^0S_{\mathrm{U}}$ and the virtual stretch rate: $\delta D_{ij} = [(\partial(\delta v_i))/(\partial {}^t x_j) + (\partial(\delta v_j))/(\partial {}^t x_i)]/2$. It can be seen from Equation (6) that the integrals are evaluated with respect to the current configuration. Therefore, proper transformations should be applied in order to convert the integrals into the undeformed configuration, since the initial shape of the solid is known. Such transformations are as follows: ${}^0\rho = J\,{}^t\rho$, $\mathrm{d}{}^t x_i = F_{ij}\mathrm{d}{}^0x_j$, $\mathrm{d}{}^tS = J_\gamma \mathrm{d}{}^0S$ and $\mathrm{d}{}^tV = J\mathrm{d}{}^tV$, where $J_\gamma = J\sqrt{\hat{n}_i B_{ij}^{-1}\hat{n}_j}$.

Due to the material and geometrical nonlinearities arising from this problem, a proper procedure is needed to facilitate further numerical implementation via the standard Newton–Raphson method. Linearising Equation (6) with respect to the unknown displacement field, and assuming a proper finite element discretisation, the final semi-discrete matrix form of the balance equations is obtained

$$\mathbf{M}^{(\alpha,\beta)} \cdot {}^{t+\Delta t}\ddot{\mathbf{u}}_{(\beta)} + \mathbf{K}^{(\alpha,\beta)} \cdot \Delta\mathbf{u}^{(\beta)} = \mathbf{R}^{(\alpha)} - \mathbf{F}^{(\alpha)}, \tag{7}$$

where

$$\mathbf{K}_{ij}^{(\alpha,\beta)} = \int_{{}^0V}\left(\frac{\partial \sigma_{in}}{\partial F_{jm}}F_{lm} + \sigma_{in}\delta_{jl}\right)\frac{\partial N^{(\alpha)}}{\partial {}^tx_n}\frac{\partial N^{(\beta)}}{\partial {}^tx_l}J\mathrm{d}V + \int_{{}^0V}\sigma_{ik}\frac{\partial N^{(\alpha)}}{\partial {}^tx_j}\frac{\partial N^{(\beta)}}{\partial {}^tx_k}J\mathrm{d}V,$$

$$\mathbf{M}_{ij}^{(\alpha,\beta)} = {}^0\rho\int_{{}^0V}\delta_{ij}N^{(\alpha)}N^{(\beta)}\mathrm{d}V,$$

$$\mathbf{R}_i^{(\alpha)} = \int_{{}^0S_{\mathrm{T}}} N^{(\alpha)}\bar{t}_i J_\gamma \mathrm{d}S, \quad F_i^{(\alpha)} = \int_{{}^0V}\sigma_{ij}\frac{\partial N^{(\alpha)}}{\partial {}^tx_j}J\mathrm{d}V.$$

In the above Jacobian matrix $\mathbf{K}$, it is assumed that no follower external forces are present, where the first integral corresponds to the material tangent stiffness and the second integral is called the geometric stiffness. $\mathbf{M}$ accounts for the consistent mass matrix, whereas $\mathbf{R}$ and $\mathbf{F}$

Downloaded by [FORTH] at 05:27 28 July 2015

are the external and internal force vectors, respectively. Further details on the linearisation steps required as well as the calculation of the tangent stiffness tensor components are provided in Appendix A.

Using the trapezoidal rule of time integration (Bathe 2007), the following assumptions are made for the velocity and displacement vector field at time $t + \Delta t$, respectively,

$$^{t+\Delta t}\dot{\mathbf{u}} = {}^{t}\dot{\mathbf{u}} + \frac{\Delta t}{2}({}^{t}\ddot{\mathbf{u}} + {}^{t+\Delta t}\ddot{\mathbf{u}}), \tag{8}$$

$$^{t+\Delta t}\mathbf{u} = {}^{t}\mathbf{u} + \frac{\Delta t}{2}({}^{t}\dot{\mathbf{u}} + {}^{t+\Delta t}\dot{\mathbf{u}}), \tag{9}$$

while within each Newton–Raphson iteration step the displacement vector is updated according to the relation: $^{t+\Delta t}\mathbf{u}^{(\kappa)} = {}^{t+\Delta t}\mathbf{u}^{(\kappa-1)} + \Delta\mathbf{u}$, where $\kappa$ is the iteration index. It is also assumed that the time increment $\Delta t$ is constant and that at the first iteration of a time step: $^{t+\Delta t}\mathbf{u}^{(0)} = {}^{t}\mathbf{u}$.

By substituting the previous relations into Equation (7), then the following equation is obtained

$$\left[\frac{4}{\Delta t^2}\mathbf{M}^{(\alpha,\beta)} + \mathbf{K}^{(\alpha,\beta)}\right] \cdot \Delta\mathbf{u}^{(\beta)} = \mathbf{R}^{(\alpha)} - \mathbf{F}^{(\alpha)} + \frac{4}{\Delta t^2}\mathbf{M}^{(\alpha,\gamma)} \cdot \left[{}^{t}\mathbf{u}^{(\gamma)} + \Delta t\,{}^{t}\dot{\mathbf{u}}^{(\gamma)} + \frac{\Delta t^2}{4}{}^{t}\ddot{\mathbf{u}}^{(\gamma)} - {}^{t+\Delta t}\mathbf{u}^{(\gamma,\kappa-1)}\right]. \tag{10}$$

Hence, by numerically solving Equation (10) for each Newton–Raphson iteration step and for each time step until convergence is achieved, the transient analysis ends up to the desired time of dynamic observation of the nonlinear system.

The numerical implementation of the present finite element procedure for the simulation of the dynamic mechanical behaviour of 3D muscles was carried out through our open-source, scalable, C++ program. The project used in this study utilises available open source numerical libraries, such as PETSc[3] (Balay et al. 2008), ParMETIS[4] (Karypis and Schloegel 2011) and libMesh[5] (Kirk et al. 2006).

## 3. Results

Dynamic simulations of the squid arm extension and frog gastrocnemius muscle contraction are carried out first in order to validate the proposed methodology and the modelling assumptions are adopted. Validation is performed by comparing the computed numerical results with experimental measurements and other numerical results that are available in the literature. Next, various simulations of the octopus arm muscular hydrostat are presented, in which different muscle groups activation and various activation patterns are performed in order to enhance our understanding of the underlying muscle mechanics in the octopus arm manoeuvre ability.

### 3.1 *Dynamic squid arm extension*

The first numerical example involves the dynamic extension of a squid arm during the strike to catch prey. The squid arm consists of an active stalk and a passive club, as depicted in Figure 1(b), having 93 mm total length. For simplicity, the squid arm is modelled as a cylindrical body. The stalk composes of 15% longitudinal muscles having fibre orientation along the $z$-axis (represented by an outer 0.3 mm thickness layer), and an inner cylindrical core of transverse muscles of 3.4 mm radius (see Figure 1(a)). The club is considered in the present analysis to have the same muscular structure as in the stalk but it is taken to behave passively. Detailed description of the squid musculature is given by Van Leeuwen and Kier (1997). The material properties of the muscle fibres and connective tissues are identical to those used by previous investigators (Johansson et al. 2000; Liang et al. 2006), while the applied activation signal for the current simulation is the following time step function

$$f^{(a)} = \begin{cases} \left[\frac{1}{2}(1 + \sin((\pi t)/t_a - \pi/2))\right]^{15}, & t \le t_a, \\ 1, & t > t_a, \end{cases}$$

where the signal peak-value time is set as $t_a = 40$ ms. In the present analysis, the dynamic simulation time was set as $t_d = 0.07$ s and the time step for implicit time integration scheme was set as $\Delta t = 0.25 \times 10^{-6}$ s. However,

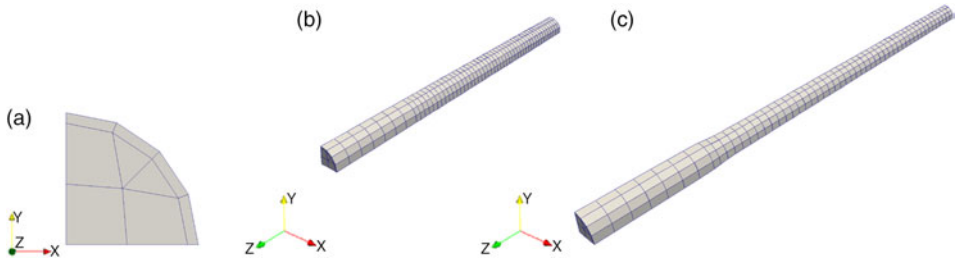


Figure 1. (a) Finite element discretisation of the quarter cross section of squid arm, with (b) initial (undeformed) configuration and (c) final (deformed) shape of the squid arm during the strike to catch prey simulation.

Downloaded by [FORTH] at 05:27 28 July 2015

for comparison purposes, the same simulation was carried out via an explicit time integration scheme (refer to Section 9.5.1 in Bathe 2007), where the time step was limited to $\Delta t = 0.005 \times 10^{-6}$ s due to numerical stability constraints. Note that even though explicit time stepping does not require any iterative procedures, the total CPU time for the explicit time-marching simulations is larger especially for cases in which it is necessary to use very small elements for accurate representation of geometrical details.

Due to symmetry, only one quadrant of the cylindrical arm is modelled and appropriate boundary conditions are applied to the symmetry planes; the surface on the root of the arm is restricted to move axially, whereas the rest of the boundary is traction free. Discretisation is accomplished with the aid of the open source mesh generator Gmsh (Geuzaine and Remacle 2009). The mesh consists of 371 eight-node hexahedral and 106 six-node triangular-base prismatic elements (see Figure 1).

As the activation signal $f^{(a)}$ increases, transverse muscles contract resulting in the axial arm deformation. In order to maintain constant volume, the radius of the arm decreases whereas the length of the arm increases. After 50 ms of full activation, the passive tensile forces of the longitudinal muscles are greater than the contractile active forces of the transverse muscles. Thus, it leads to extension deceleration and finally to manoeuvre termination. The final deformed squid arm is depicted in Figure 1(c).

Figure 2(a) shows the squid arm length growth in time. The finite element numerical results, obtained by the current methodology (black solid line), are compared with the experimental data (red empty diamonds) of the squid arm extension and the corresponding 1D model simulations (blue solid line) obtained by Van Leeuwen and Kier (1997). In view of Figure 2, it is observed that the FEM numerical results agree very well both qualitatively and quantitatively with those of Van Leeuwen and Kier (1997). However, in Figure 2(b) it can be noted that a relatively lower arm tip velocity is evaluated through the proposed analysis. It is interesting to note that similar behaviour was observed by other FEM approaches (Johansson et al. 2000; Liang et al. 2006; Tang et al. 2009). Furthermore, the dynamic extension of the squid arm was solved by utilising an explicit finite element solver. As it is depicted in Figure 2, both explicit and implicit approaches provide relatively identical estimations of the squid arm axial length and arm tip velocity, but the implicit solver advances in time with a step 50 times larger. As a result, the CPU time for the finite element simulations in Figure 2 (until final simulation time $t_d = 0.07$ s) was approximately 34 h for the implicit solver, and approximately 59 h for the explicit solver.

In order to examine for the numerical scheme $h$-refinement convergence, the dynamic squid arm extension problem was solved for another two finer finite element discretisations. The obtained numerical results (not presented herein) agree very well with the results given in Figure 2 computed on a coarser mesh. Furthermore, the dynamic squid arm extension was simulated for various values of the time step $\Delta t$, where it was verified that the numerical results converge. However, when the time step increases significantly then hour-glassing deformations are observed, which are due to the reduced integration scheme incorporated in order to avoid elements' volumetric locking.

### 3.2 Frog gastrocnemius muscle

In this subsection, the deformation of the frog gastrocnemius muscle, which is subject to activation and under a constant tensile load along the muscle fibre direction, is simulated. The assumed muscle geometry is provided in Tang et al. (2007), while the material parameters are adopted from their successive work (Tang et al. 2009). In these studies, a Hill three-element model is utilised in order to describe the mechanical behaviour of skeletal muscles. To this end, analytical evaluation of the Cauchy stress tensor and tangent stiffness tensor in the fibre and connective tissue level is carried out, and it is presented in Appendix B. The activation load is identical to that of Tang et al. (2009), and similar boundary conditions are considered. However, in the present simulation, muscles, fatigue is not taken into account. The finite element discretisation of the frog gastrocnemius muscle – comprising 480 eight-node hexahedral elements – is depicted in Figure 3(a). The fibre orientation is defined by the local axial direction of each finite element, which follows the fusiform geometry of the muscle. In Figure 3(b), the final deformed body of the muscle is also presented.

In Figure 4, comparison of the deformed shape outline of the frog muscle at maximum activation level on the $x-z$ and $y-z$ planes is shown. In this figure, the experimental results obtained by Tang et al. (2007) and their numerical results at the first activation circle with the numerical results of the present finite element procedure are compared. The numerical results in both finite element approaches are in relatively good agreement with the experimental measurements.

### 3.3 Octopus muscular hydrostat dynamic simulations

Assume a conical geometry of the octopus arm extending along the $z$-axis, being 10 cm long and having 1 cm root diameter. The arrangement of muscles in the octopus muscular hydrostat is very different compared to that of the squid arm (Kier and Stella 2007), and is depicted in Figure 5(a). The arm musculature consists mainly of longitudinal muscles (denoted with 'L' in Figure 5(a)) that extend along the arm axial direction and transverse muscles (denoted with 'T') that connect the external connective tissues with the longitudinal muscles and the axial nerve cord (denoted with 'N'). In addition, oblique muscles are present (denoted with 'O'), which are helically aligned fibres around the arm, thus enabling arm torsion. For the

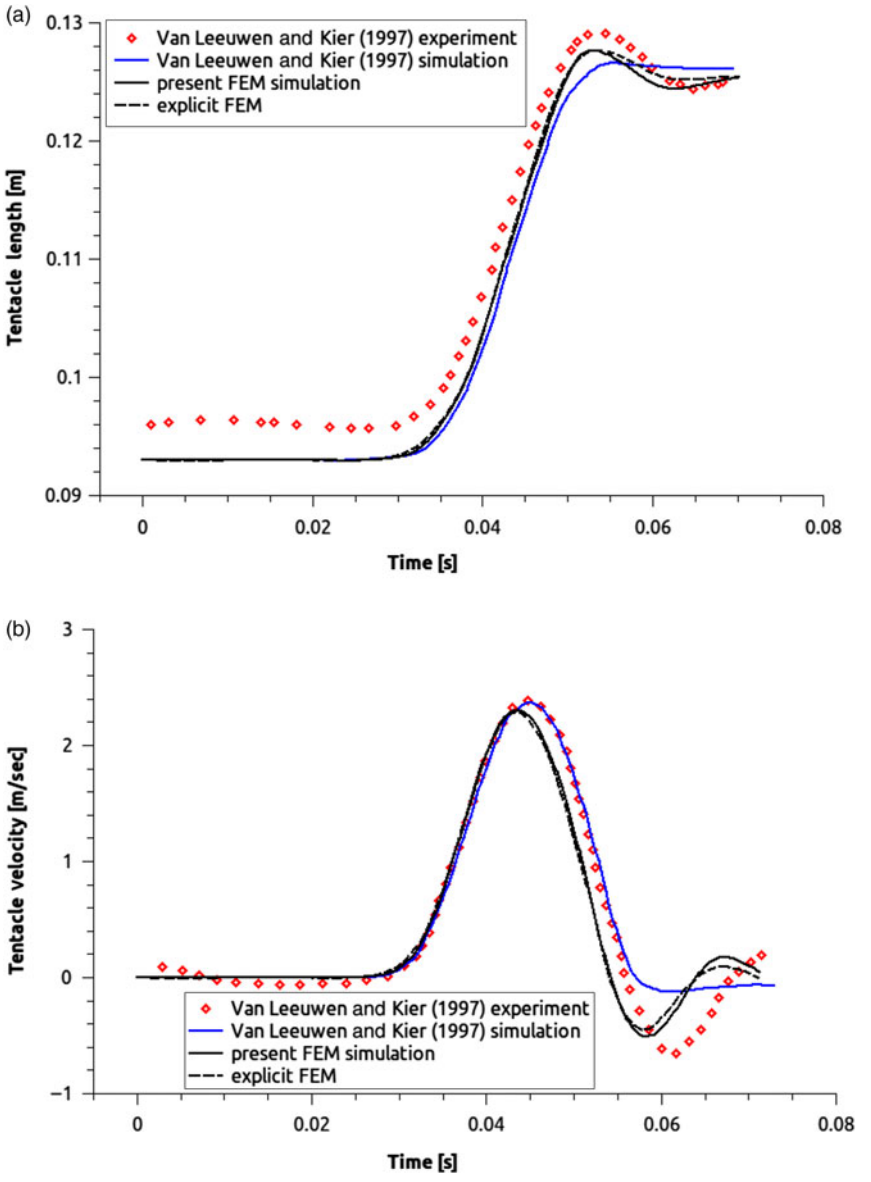


Figure 2. Comparison of experimental and simulation results of the squid: (a) arm length and (b) arm-tip velocity profile.

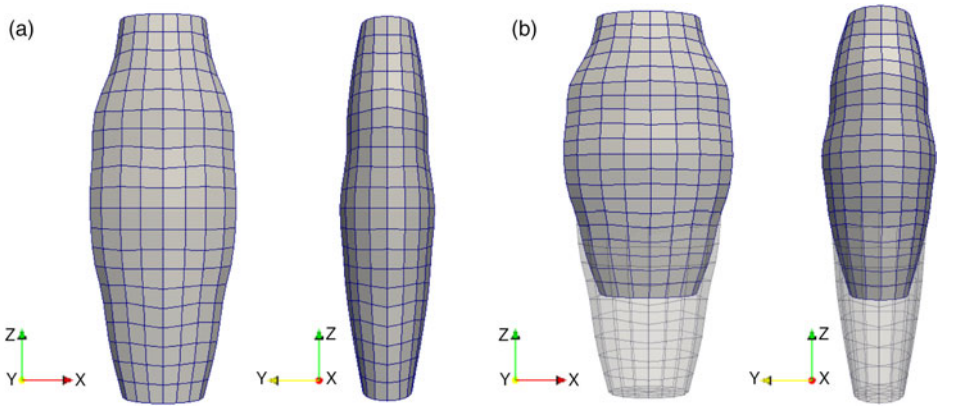


Figure 3. (a) Finite element discretisation of the undeformed frog muscle and (b) final deformed geometry.

Downloaded by [FORTH] at 05:27 28 July 2015

Downloaded by [FORTH] at 05:27 28 July 2015

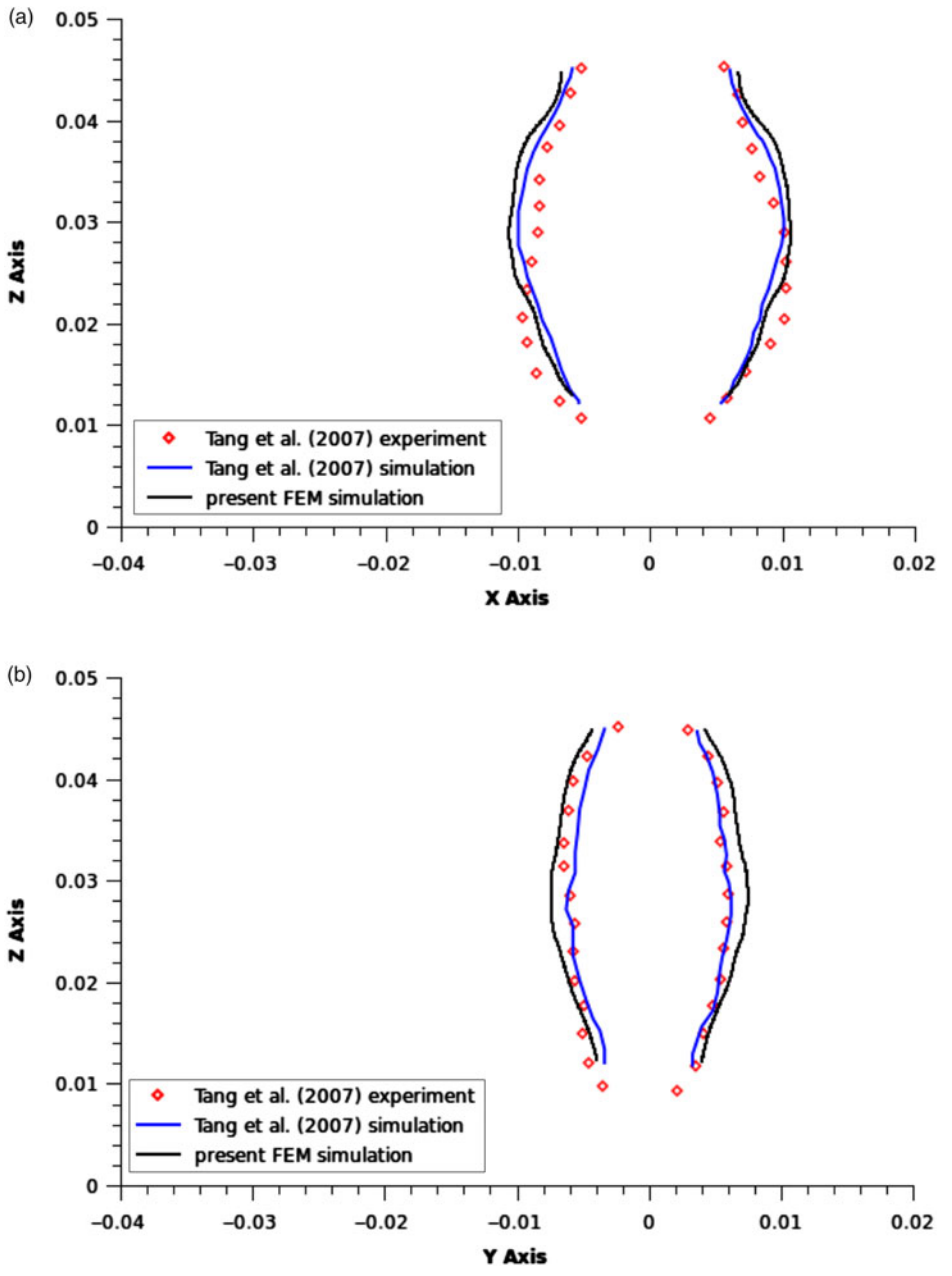


Figure 4. Deformed shape outline of the frog gastrocnemius muscle and comparison of the experimental and simulation results on the (a) $x-z$ and (b) $y-z$ planes.

present analyses, oblique muscles are omitted because their contribution to bending motion of the octopus arm is expected to be minor (Yekutieli et al. 2005; Liang et al. 2006).

The lack of experimental data on the octopus muscular hydrostat material properties restricts us to utilise the corresponding data of the squid, which are provided in the paper of Van Leeuwen and Kier (1997). This assumption is based on the fact that both molluscs are of the same class (Cephalopoda), despite their arm of different muscular structures.

The finite element mesh of the octopus arm consists of 420 eight-node hexahedral and 420 six-node triangular-base prismatic elements, as seen in Figure 5(b). On the top left of Figure 5(b), the two main muscular kinds of longitudinal and transverse muscles – shaded with different colours – that are considered in the octopus arm are depicted. Hence, following Figure 5(a), the longitudinal muscles are taken as four distinctive groups (green-colour subregions), thus enabling them for separate activation, whereas the transverse muscles are located in the core of the idealised conical octopus arm (yellow-colour subregions). Clearly, the very

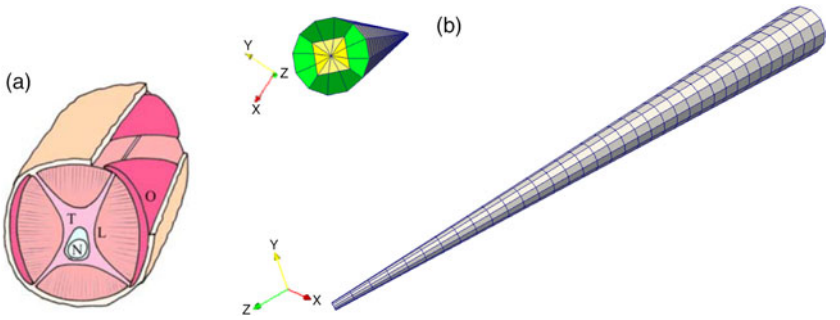


Figure 5. (a) Diagram of the octopus arm showing the arrangement of muscle fibres and connective tissues. (b) Finite element discretisation of the octopus arm and close-up view of the arm root seen on the top left.

small elements at the tip of the arm, required for accurate representation of the geometry, are expected to impose very severe stability limitations to explicit time integration schemes. Therefore, all simulations for the octopus arm were carried out by using the implicit time-marching scheme.

The wet area of the arm is considered traction free, whereas the root of the arm is allowed to move on the $x$–$y$ plane and is fixed at two points in order to avoid rigid body motion. The octopus arm simulations were carried out by assuming the following activation time function:

$$f^{(a)} = \begin{cases} 0, & t \le t_i, \\ \left[\frac{1}{2}(1+\sin((\pi t/t_a)-\pi/2))\right]^{3.5}, & t \le t_i + t_a, \\ 1, & t \le t_i + t_d, \\ \mathrm{e}^{-S(t-t_i-t_d)}, & t > t_i + t_d, \end{cases}$$

where the activation signal peak-value time is set as $t_a = 0.5$ s, while $t_i$ and $t_d$ are the initialisation and duration time of the activation function, respectively, and $S = 20$.

### 3.3.1 *One longitudinal muscle activation*

In order for the octopus arm to perform a bending manoeuvre, longitudinal muscles have to be activated primarily (Liang et al. 2006), while transverse muscles behave passively. To this end, it is assumed that one group (subregion) of longitudinal muscles is activated uniformly ($t_i = 0$) or non-uniformly ($t_i = \bar{z}$), where $\bar{z}$ is the normalised axial position of a material point within the undeformed arm muscular hydrostat. Non-uniform activation occurs due to the variable $t_i$ in respect with the axial position of a muscle fibre material point. The total time duration of the activation level is set as $t_d = 1$ s in both cases.

Successive snapshots of the arm deformation are presented in Figure 6, in which the transparent grey area corresponds to the undeformed octopus arm. As seen in this figure, the octopus arm performs the bending manoeuvre within 0.5 s of full activation level and then it oscillates slightly to this equilibrium position until simulation termination. It is important to note here that no external forces are considered in the present analysis, such as hydrodynamic forces exerted by the surrounding water (Yekutieli et al. 2005; Kazakidi et al. 2012), which could influence the dynamic octopus arm bending manoeuvre. However, hydrodynamic forces can be easily incorporated into the present formulation.

In Figure 7, various snapshots of the octopus arm bending procedure are presented, where non-uniform activation of one longitudinal muscle group takes place. As expected, the arm deforms rather slowly and requires more time to bend than in the uniform activation case. This is explained by the fact that until 0.25 s simulation time only the first quarter of the longitudinal subregion is fully activated (from $z = 0$ up to 0.025 m), whereas until 0.5 s only the first half of the longitudinal subregion is fully activated and so on. We also carried out simulations for non-uniform activation of one longitudinal subregion with initialisation time $5\bar{z}$ and $2\bar{z}$ (not presented herein) but the arm deformation is very slow and the final bend is not achieved within 1 s of simulation time.

### 3.3.2 *Two longitudinal muscles activation*

Next, an octopus arm off-plane bending is simulated. Since circumferential muscles were not taken into account in this study, one way to achieve torsion to the arm is to enforce the stimulation of two neighbouring longitudinal muscular groups by applying a proper time lag. More precisely, the first muscular group is activated non-uniformly ($t_i = \bar{z}$) with activation signal peak-value time $t_a = 0.5$ s, as in Section 3.3.1, whereas the second muscular group is activated non-uniformly ($t_i = \bar{z}$) but only a small portion along the $z$-axis of the arm (from the root $z = 0$ up to $z = 3$ cm) is active.

In Figure 8, various representative snapshots of the octopus arm deformation during the off-plane bending are presented in successive order until manoeuvre termination. From Figure 8(a)–(j), it is evident that the arm follows a deformation path identical to the non-uniform activation of one longitudinal muscle simulation case. However, after full activation of the neighbouring muscle at 1 s, the arm seems to exhibit some twisting effects (see Figure 8(l)–(x)), which are more pronounced at $t = 1.125$ (see Figure 8(r)).

Downloaded by [FORTH] at 05:27 28 July 2015

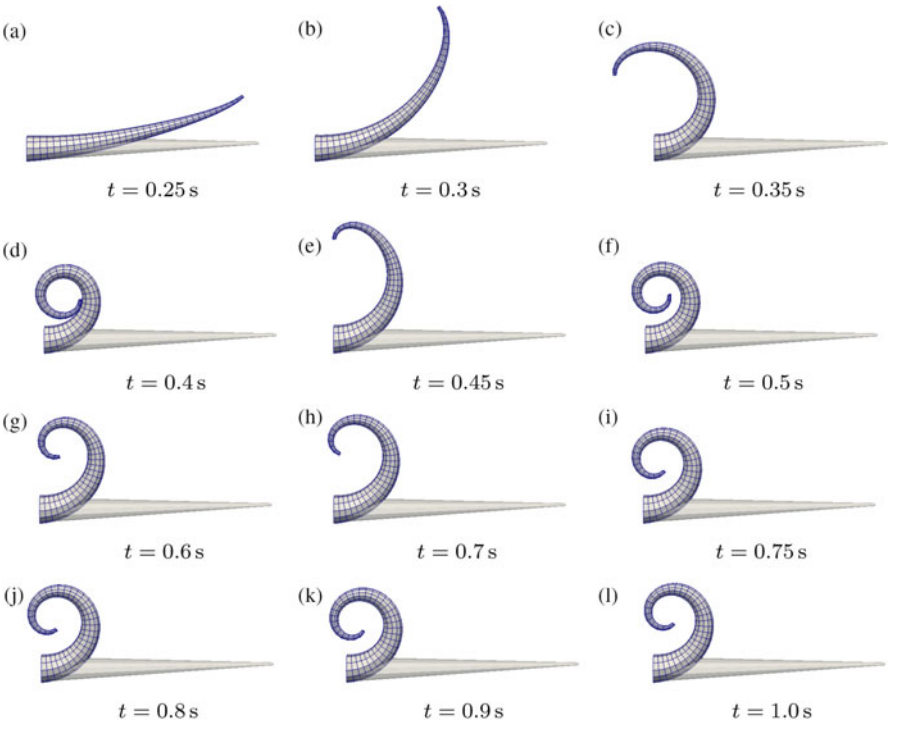


Figure 6. Various snapshots of the octopus arm deformation for uniform activation of one longitudinal muscle group.

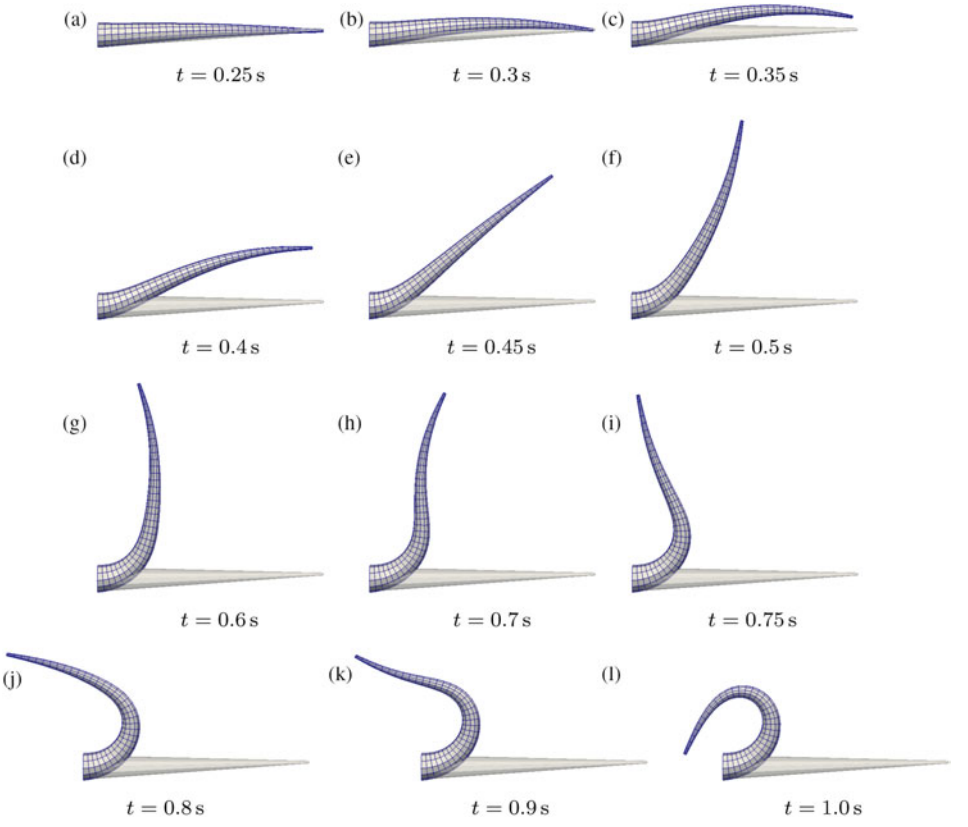


Figure 7. Various snapshots of the octopus arm deformation for non-uniform activation of one longitudinal muscle group.

Downloaded by [FORTH] at 05:27 28 July 2015

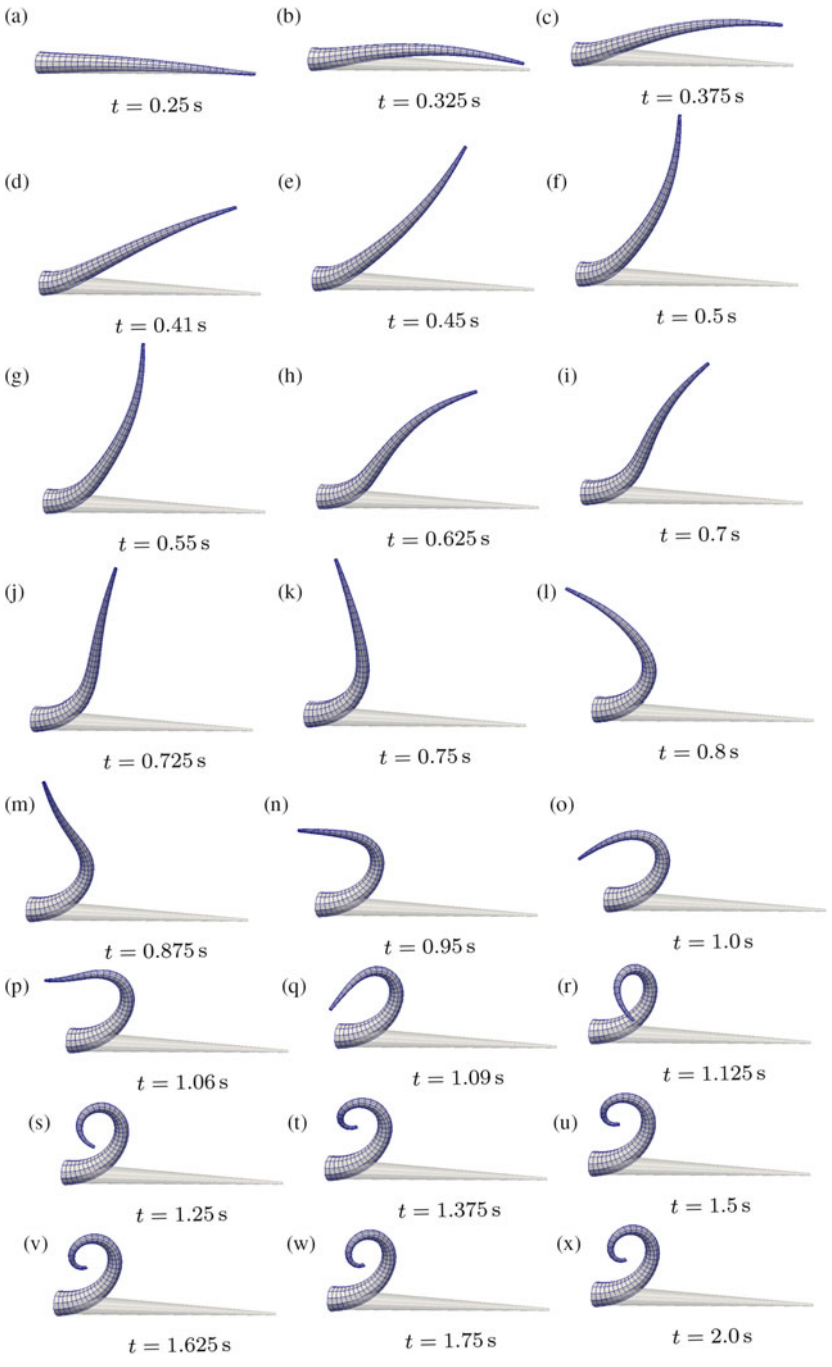


Figure 8. Various snapshots of the octopus arm deformation during an off-plane bending manoeuvre.

Due to the fact that no damping mechanisms were considered into the finite element model, the octopus arm is observed to exhibit oscillations at the late stage of the manoeuvre termination, e.g. within $t = 1.4 - 1.9$ s. It is important to note here that if circumferential muscles were considered in the FEM simulations, it would be expected for the arm to achieve significant torsion, in which the contraction of these helically aligned muscles would also result into arm elongation.

### 3.3.3 *All longitudinal muscles' activation*

In this paragraph, it is aimed for the numerical simulation of two primitive octopus arm manoeuvres, i.e. bending and reaching in consecutive fashion. In order to achieve this, the longitudinal muscles are activated separately in pairs of two. Firstly, a uniform activation ($t_i = 0$) of two neighbouring longitudinal muscular groups is enforced, having activation signal peak-value time $t_a = 0.5$ s and duration time $t_d = 2$ s (see red solid line in Figure 9),

Downloaded by [FORTH] at 05:27 28 July 2015

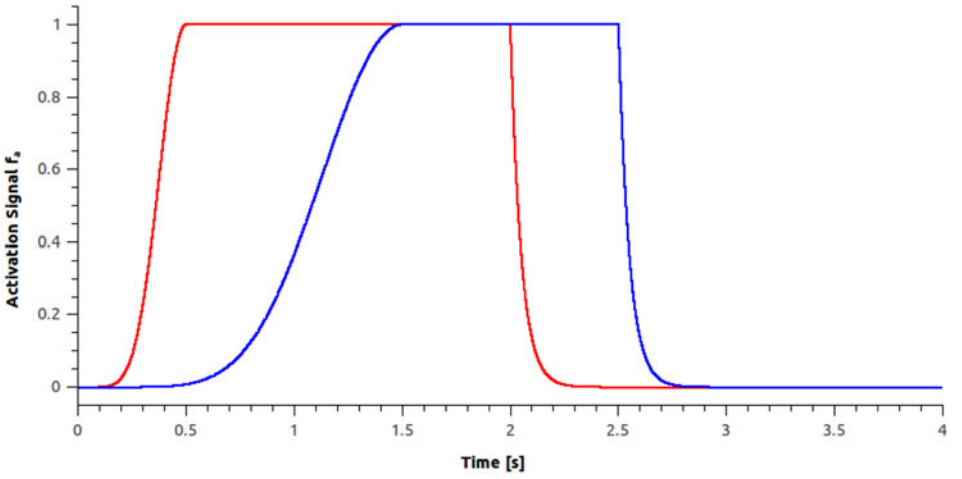


Figure 9. Activation signals occurring for the two pairs of longitudinal muscles.

Downloaded by [FORTH] at 05:27 28 July 2015

in which only a portion of the arm is stimulated (from $z = 2$ cm up to the tip $z = 10$ cm). Next, the rest of the two neighbouring longitudinal muscular groups are activated non-uniformly ($t_i = \bar{z}$) having activation signal peak-value time at $t_a = 1.5$ s and duration time $t_d = 2.5$ s (see blue solid line in Figure 9).

In Figure 10, various representative snapshots of the octopus arm deformation during the bending and reaching manoeuvre are presented in successive order. As seen in Figure 10(a)–(d), the first two longitudinal muscle groups are activated, thus resulting into the arm bending depicted in these figures. However, the bent shape of the arm is less pronounced in this case (see Figure 10(c)), as compared with the simulation example of Section 3.3.1 (see Figure 6(l)), because 80% of the arm longitudinal muscles are active. In addition, due to the lack of damping in the mechanical nonlinear system, the arm exhibits some oscillation from 0.7 s up to 1 s. Furthermore, the contraction of the rest of the longitudinal muscles results in the oscillation decrease and further to arm bending on the opposite direction, since the latter group of muscles is activated all along the arm. This is also evident from Figure 10(e)–(q), in which a rather slow bend occurs since non-uniform activation is applied to the other two longitudinal muscles. In conjunction with Figures 9 and 10(n)–(q), it can be seen that the activation of the second pair of longitudinal muscles and the full deactivation of the first pair of longitudinal muscles provide a similar hook-like arm deformation (compare Figure 10(c),(p)). Finally, that the gradual recovery of the octopus arm to its undeformed shape can be observed in Figure 10(q)–(x), which is due to the deactivation of the second group of longitudinal muscles. It is important to note that the reader should not get confused with Figure 9, where $t_d = 2.5$ s since the deactivation of the second pair of longitudinal muscles is non-uniform; thus, the true time duration of the activation signal before decay is $t_i + t_d = \bar{z} + 2.5$ s.

## 4. Conclusions

In this study, a nonlinear dynamic finite element procedure for simulating biological muscle mechanics is presented. The proposed numerical method is capable of simulating the dynamic mechanical behaviour of 3D, nonlinear, nearly incompressible, hyperelastic materials – such as muscular hydrostats – that undergo large deformations. The muscle is considered as a homogeneous continuous medium, consisting of connective tissues and fibres. The former part is described through a Mooney–Rivlin constitutive model, whereas the latter part is considered to be the sum of active and passive stresses. The nonlinear equations of dynamic equilibrium are solved via the Newton–Raphson iterative procedure, and time integration is performed through an implicit scheme. The validity of the proposed methodology is demonstrated with two representative numerical examples, whereas the efficiency and ability of the FEM to simulate octopus arm manoeuvres are demonstrated through a series of numerical simulations. The proposed methodology can successfully simulate primitive arm motions of muscular hydrostats more accurately and efficiently, compared to previous approaches (Yekutieli et al. 2005; Liang et al. 2006).

In future developments, oblique muscles of the octopus arm could be accounted for, and introduction of external hydrodynamic forces during the arm movement could allow to produce more realistic simulations. In addition, utilisation of higher order elements and *p*-adaptive procedures could help to increase the accuracy of simulated transient motions, in order to overcome any hour-glassing deformation deficiencies. Research work is underway which would simulate more realistic octopus arm motions, such as the reaching manoeuvre evoked by a bend-like propagation activation pattern, as in Yekutieli et al. (2005). These activation patterns could be identified by imposing the desired shape deformation time history, thus evaluating the

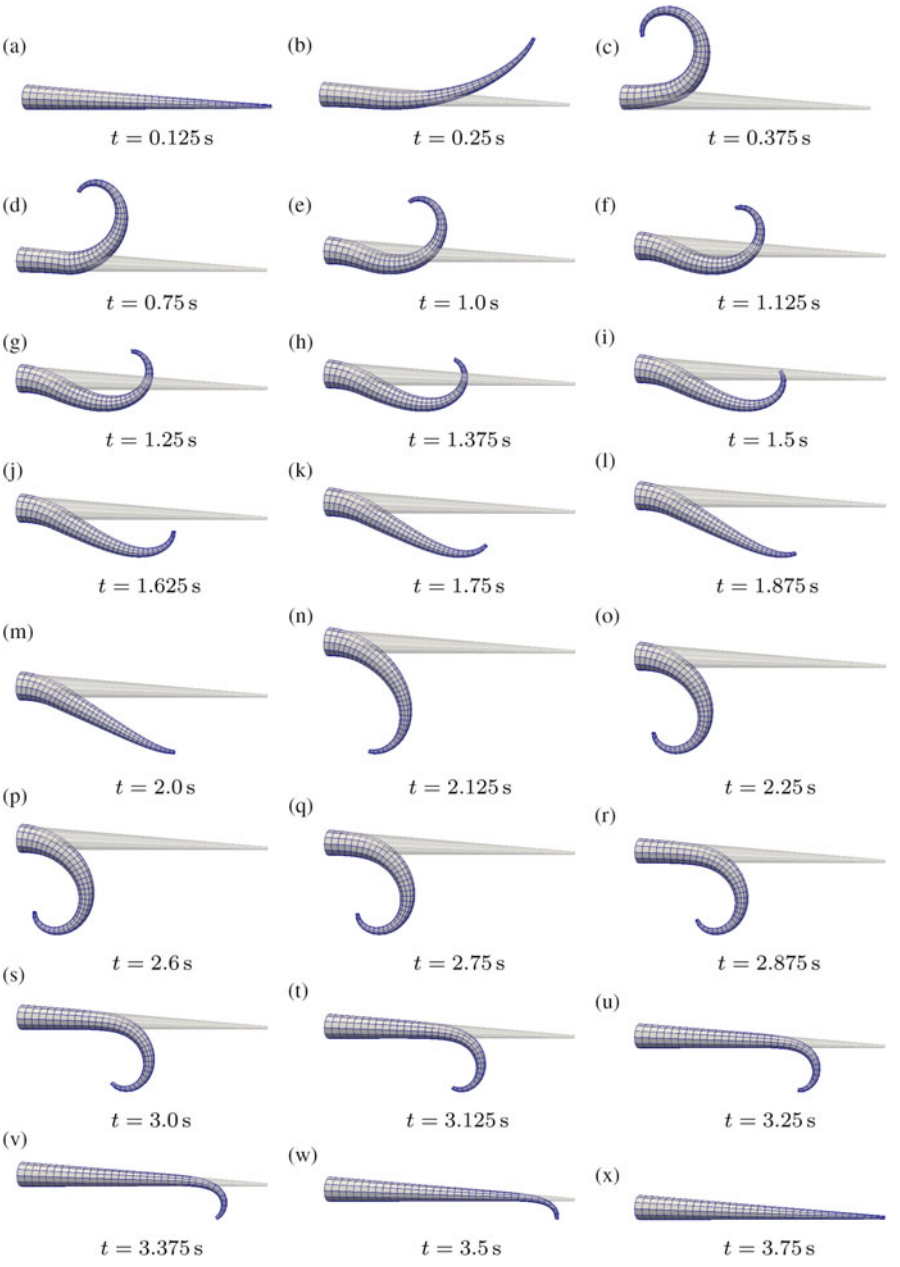


Figure 10. Various snapshots of the octopus arm deformation during the bending and reaching manoeuvre.

required loadings that subsequently would yield the desired activation function.

## Acknowledgement

The authors gratefully acknowledge the support by the OCTOPUS IP project with number FP7-231608.

## Notes

1. Present address: Department of Civil and Environmental Engineering, University of Cyprus, Nicosia 1678, Cyprus.
2. http://www.octopusproject.eu/index.html.
3. http://www.mcs.anl.gov/petsc/petsc-as/.
4. http://glaros.dtc.umn.edu/gkhome/metis/parmetis/overview.
5. http://libmesh.sourceforge.net/.

## References

Balay S, Buschelman K, Eijkhout V, Gropp WD, Kaushik D, Knepley MG, Curfman McInnes L, Smith BF, Zhang H. 2008. PETSc users manual. ANL-95/11 – Revision 3.0.0, Argonne National Laboratory.

Bathe K-J. 2007. Finite element procedures. Prentice Hall, ISBN-10: 097900490X.

Downloaded by [FORTH] at 05:27 28 July 2015

Beskos DE, Jenkins JT. 1975. A mechanical model for mammalian tendon. J Appl Mech. 42:755–758.
Bower AF. 2009. Applied mechanics of solids. CRC Press, ISBN-10: 1439802475.
Fernandez JW, Buist ML, Nickerson DP, Hunter PJ. 2005. Modelling the passive and nerve activated response of the rectus femoris muscle to a flexion loading: a finite element framework. Med Eng Phys. 27:862–870.
Fung YC. 1993. Biomechanics: mechanical properties of living tissues. 2nd ed. Springer-Verlag, ISBN-10: 0387979476.
Geuzaine C, Remacle J-F. 2009. Gmsh: a three-dimensional finite element mesh generator with built-in pre- and post-processing facilities. Int J Numer Meth Eng. 79:1309–1331.
Hill AV. 1938. The heat of shortening and the dynamic constants of muscle. Proc Royal Soc London Ser B, Biol Sci. 126: 136–195.
Holzapfel GA. 2000. Nonlinear solid mechanics: a continuum approach for engineering. Wiley, ISBN-10: 0471823198.
Humphrey JD, Yin FCP. 1987. On constitutive relations and finite deformations of passive cardiac tissue: I. A pseudo-strain-energy function. J Biomech Eng. 109:298–304.
Huxley AF. 1957. Muscle structure and theories of contraction. Prog Biophys Mol Biol. 164:255–318.
Johansson T, Meier M, Blickhan R. 2000. A finite-element model for the mechanical analysis of skeletal muscles. J Theor Biol. 206:131–149.
Karypis G, Schloegel K. 2011. ParMETIS: Parallel Graph Partitioning and Sparse Matrix Ordering Library. Version 4.0, University of Minnesota, Department of Computer Science and Engineering, Minneapolis.
Kazakidi A, Vavourakis V, Pateromichelakis N, Ekaterinaris JA, Tsakiris DP. 2012. Hydrodynamic Analysis of Octopus-like Robotic Arms. IEEE International Conference on Robotics and Automation (ICRA), St. Paul, Minnesota, USA.
Kier WM, Stella MP. 2007. The arrangement and function of octopus arm musculature and connective tissue. J Morphol. 268:831–843.
Kirk B, Peterson JW, Stogner RH, Carey GF. 2006. libMesh: a C++ library for parallel adaptive mesh refinement/coarsening simulations. Eng Comp. 22:237–254.
Kojic M, Mijailovic S, Zdravkovic N. 1998. Modelling of muscle behavior by the finite element method using Hill's three-element model. Int J Numer Meth Eng. 43:941–953.
Liang Y, McMeeking RM, Evans AG. 2006. A finite element simulation scheme for biological muscular hydrostats. J Theor Biol. 242:142–150.
Lu YT, Zhu HX, Richmond S, Middleton J. 2010. A visco-hyperelastic model for skeletal muscle tissue under high strain rates. J Biomech. 43:2629–2632.
Martins JAC, Pires EB, Salvado R, Dinis PD. 1998. A numerical model of passive and active behavior of skeletal muscles. Comp Meth Appl Mech Eng. 151:419–433.
Martins JAC, Pato MPM, Pires EB. 2006. A finite element model of skeletal muscles. Virtual Phys Prototyping. 1:159–170.
Mooney M. 1940. A theory of large elastic deformation. J Appl Phys. 11:582–592.
Nigg BM, Herzog W. 1999. Biomechanics of the musculo-skeletal system. 2nd ed. Wiley, ISBN-10: 0471978183.
Oomens CWJ, Maenhout M, Van Oijen CH, Drost MR, Baaijens FP. 2003. Finite element modelling of contracting skeletal muscle. Phil Trans Royal Soc B: Biol Sci. 358: 1453–1460.
Röhrle O, Pullan AJ. 2007. Three-dimensional finite element modelling of muscle forces during mastication. J Biomech. 40:3363–3372.
Stojanovic B, Kojic M, Rosic M, Tsui CP, Tang CY. 2007. An extension of Hill's three-component model to include different fibre types in finite element modeling of muscle. Int J Numer Meth Eng. 71:801–817.
Tang CY, Tsui CP, Stojanovic B, Kojic M. 2007. Finite element modelling of skeletal muscles coupled with fatigue. Int J Mech Sci. 49:1179–1191.
Tang CY, Zhang G, Tsui CP. 2009. A 3D skeletal muscle model coupled with active contraction of muscle fibres and hyperelastic behavior. J Biomech. 42:865–872.
Van Leeuwen JL. 1991. Optimum power output and structural design of sarcomeres. J Theor Biol. 149:229–256.
Van Leeuwen JL, Kier WM. 1997. Functional design of tentacles in squid: linking sarcomere ultrastructure to gross morphological dynamics. Phil Trans Royal Soc B: Biol Sci. 352: 551–571.
Yekutieli Y, Sagiv-Zohar R, Aharonov R, Engel Y, Hochner B, Flash T. 2005. Dynamic model of the octopus arm. I. Biomechanics of the octopus reaching movement. J Neurophys. 94:1443–1458.
Zajac FE. 1989. Muscle and tendon: properties, models, scaling and application to biomechanics and motor control. CRC Critical Rev Biomed Eng. 17:359–411.
Zienkiewicz OC, Taylor RL. 2005. The finite element method for solid and structural mechanics. 6th ed. Butterworth-Heinemann, ISBN-10: 0750663219.

Downloaded by [FORTH] at 05:27 28 July 2015

Downloaded by [FORTH] at 05:27 28 July 2015

## Appendix A. Finite element linearisation steps

The stress equilibrium equation can be replaced by the equivalent principle of virtual work that accounts for finite deformations, and it can be given in terms of the Kirchhoff stress measure $\tau_{ij}$. The virtual work equation can be expressed into the reference configuration (Bower 2009) as

$$\delta\Pi = \int_{0_V} \delta L_{ij}\tau_{ij}\mathrm{d}V - \int_{0_{S_T}} \delta v_i \bar{t}_i J_\gamma \mathrm{d}S = 0, \tag{A1}$$

where for simplicity the inertia term is removed.

Inserting proper finite element interpolation polynomials into Equation(A1), where unknown kernel quantities are interpolated via Lagrange polynomial bases: ${}^0x_i = \sum_\alpha N^{(\alpha)}\,{}^0x_i^{(\alpha)}$, $\partial u_i/\partial {}^t x_j = \sum_\alpha [\partial N^{(\alpha)}/\partial {}^t x_j] u_i^{(\alpha)}$, and given that the virtual velocity gradient matrix can be written in the form: $\delta L_{ij} = (\partial(\delta v_i))/(\partial {}^t x_j) = [(\partial(\delta v_i)/\partial {}^0 x_t)]F_{kj}^{-1}$, it follows that

$$\delta v_i^{(\alpha)} \left\{ \int_{0_V} \frac{\partial N^{(\alpha)}}{\partial {}^0 x_k} F_{kj}^{-1} \sigma_{ij} J \mathrm{d}V - \int_{0_{S_T}} N^{(\alpha)} \bar{t}_i J_\gamma \mathrm{d}S \right\} = 0. \tag{A2}$$

In order to solve the above discrete nonlinear virtual work equation using the Newton–Raphson procedure, a corrected updated solution $u_i^{(\alpha)} + \Delta u_i^{(\alpha)}$ is assumed, where $u_i^{(\alpha)}$ is the solution at the end of the preceding time increment or the previous iteration solution. Given the fact that no follower external forces are present in the current analysis, Equation (A2) becomes

$$\int_{0_V} \frac{\partial N^{(\alpha)}}{\partial {}^0 x_k} [F + \Delta F]_{kj}^{-1} \sigma_{ij} J \mathrm{d}V = \int_{0_{S_T}} N^{(\alpha)} \bar{t}_i J_\gamma \mathrm{d}S, \tag{A3}$$

where the above Cauchy stress tensor $\sigma_{ij}$ and deformation gradient determinant $J$ are also dependent on that increment.

Linearising the left-hand side integral of Equation (A3) by using a consistent Newton–Raphson iteration procedure, and following the linearisation steps presented in the book of Bower (2009) (refer to Subsection 8.4.4), the following equation can be obtained

$$\left\{ \int_{0_V} \left[ C_{ijkl} \frac{\partial N^{(\alpha)}}{\partial {}^0 x_r} F_{rj}^{-1} \frac{\partial N^{(\beta)}}{\partial {}^0 x_s} F_{sl}^{-1} - \sigma_{ij} \frac{\partial N^{(\alpha)}}{\partial {}^0 x_m} F_{mk}^{-1} \frac{\partial N^{(\beta)}}{\partial {}^0 x_n} F_{nj}^{-1} \right] J \mathrm{d}V \right\} \Delta u_k^{(\beta)} = \int_{0_{S_T}} N^{(\alpha)} \bar{t}_i J_\gamma \mathrm{d}S - \int_{0_V} \sigma_{ij} \frac{\partial N^{(\alpha)}}{\partial {}^0 x_p} F_{pj}^{-1} J \mathrm{d}V, \tag{A4}$$

where

$$C_{ijkl} = \frac{\partial \sigma_{ij}}{\partial F_{ks}} F_{ls} + \sigma_{ij}\delta_{kl}, \tag{A5}$$

the tangent stiffness fourth-order tensor.

## Appendix B. Tangent stiffness matrix and stress tensor evaluation

As discussed in Section 2, the Cauchy stress distribution at a material point within the biological muscle is considered as the superposition of stresses at the connective tissues and muscle fibres, respectively, as $\sigma_{ij} = \sigma_{ij}^{(\mathrm{ct})} + \sigma_{ij}^{(\mathrm{f})}$. Therefore, it can be safely assumed that the tangent stiffness matrix of the material in the finite element level is equal to the sum of the corresponding matrices of the connective tissues and fibres

$$C_{ijkl} = \frac{\partial \sigma_{ij}}{\partial F_{ks}} F_{ls} + \sigma_{ij}\delta_{kl} = C_{ijkl}^{(ct)} + C_{ijkl}^{(\mathrm{f})}. \tag{B1}$$

The fourth-order material tangent stiffness tensor of Equation (B1) for the connective tissues can be evaluated analytically, providing the corresponding expression of the Cauchy stress tensor (see Equation 3), which is given below

$$\begin{aligned} C_{ijkl}^{(ct)} = {} & [4/9J(c_1\bar{I}_1 + 4c_2\bar{I}_2) + K(2J-1)]\delta_{ij}\delta_{kl} \\ & - 4/3(c_1 + 2c_2\bar{I}_1 J^{-5/3}(B_{ij}\delta_{kl} + \delta_{ij}B_{kl}) \\ & + 8/3c_2 J^{-7/3}\left(B_{ij}^2\delta_{kl} + \delta_{ij}B_{kl}^2\right) \\ & + 2(c_1 + c_2\bar{I}_1)J^{-5/3}(\delta_{ik}B_{jl} + B_{il}\delta_{jk}) \\ & - 2c_2 J^{-7/3}\left(\delta_{ik}B_{jl}^2 + B_{il}^2\delta_{jk}\right) \\ & + 2c_2 J^{-7/3}(2B_{ij}B_{kl} - B_{il}B_{jk} - B_{ik}B_{jl}), \end{aligned} \tag{B2}$$

where $B_{ij}^2 = B_{ik}B_{kj}$.

For the fibre part, the Cauchy stress tensor is defined as $\sigma_{ij}^{(\mathrm{f})} = \sigma_0^m(1+\varepsilon_0^m)\hat{m}_i\hat{m}_j$. Given the fibre stress expressions (see Equations (4) and (5)), the analytical expression for the muscle fibres material tangent stiffness tensor can be derived as

$$\begin{aligned} C_{ijkl}^{(\mathrm{f})} = {} & \left(\lambda\frac{\partial\sigma^m}{\partial\varepsilon_0^m} - 2\sigma^m\right)\hat{m}_i\hat{m}_j\hat{m}_k\hat{m}_l \\ & + \sigma^m(\hat{m}_i\hat{m}_j\delta_{kl} + \delta_{ij}\hat{m}_k\hat{m}_l + \delta_{ik}\hat{m}_j\hat{m}_l + \hat{m}_i\delta_{jk}\hat{m}_l), \end{aligned} \tag{B3}$$

where $\sigma^m = \sigma_0^m(1+\varepsilon_0^m)$. The derivative of the fibre nominal stress with respect to the nominal strain $\varepsilon_0^m$ is given explicitly

$$\frac{\partial\sigma_0^m}{\partial\varepsilon_0^m} = \frac{\partial\sigma^{(\mathrm{pass})}}{\partial\varepsilon_0^m} + \sigma^{(\max)}f^{(a)}\left(\frac{\partial f^{(l)}}{\partial\varepsilon_0^m}f^{(v)} + f^{(l)}\frac{\partial f^{(v)}}{\partial\dot{\varepsilon}_0^m}\frac{1}{\Delta t}\right). \tag{B4}$$

In the previous equation, it is assumed that the nominal strain rate is approximately equal to $\dot{\varepsilon}_0^m \approx \Delta\varepsilon_0^m/\Delta t$; therefore, the quantity $\partial f^{(v)}/\partial\varepsilon_0^m$ by chain differentiation is set as $(\partial f^{(v)}/\partial\dot{\varepsilon}_0^m)/\Delta t$.

Based on the above calculations, the following differentiation identities are utilised:

$$\frac{\partial\lambda}{\partial F_{km}} = \frac{1}{\lambda}(F_{kr}\hat{n}_r)\hat{n}_m = \hat{m}_k\hat{n}_m, \tag{B5}$$

$$\frac{\partial\hat{m}_i}{\partial F_{km}} = \frac{1}{\lambda}\delta_{ik}\hat{n}_m - \frac{1}{\lambda^2}(F_{is}\hat{n}_s)\frac{\partial\lambda}{\partial F_{km}} = \frac{1}{\lambda}(\delta_{ik}\hat{n}_m - \hat{m}_i\hat{m}_k\hat{n}_m). \tag{B6}$$

By working in the same manner, one can derive the material tangent stiffness for the classical three-element Hill muscle model. Following the same notation as in Tang et al. (2007), the Cauchy stress in the fibre level is defined by the relationship

$$\sigma_{ij}^{(\mathrm{f})} = \frac{1}{J}g\bar{\lambda}(\hat{m}_i\hat{m}_j - 1/3\delta_{ij}), \tag{B7}$$

where $\bar{\lambda} = \lambda J^{-1/3}$ and $g(\bar{\lambda}) = \sigma_0 f_{\mathrm{PEE}} + \beta\mathrm{e}^{\alpha(\lambda_s - 1)} - \beta$; with $\sigma_0$ being the maximum isometric stress, $\alpha$ and $\beta$ are material parameters, $\lambda_s$ is the stretch of the Hill series elastic element and $f_{\mathrm{PEE}}$ is a pre-defined function with respect to $\bar{\lambda}$ for the Hill parallel elastic element component (Tang et al. 2009).

The corresponding fourth-order material tangent stiffness tensor for the muscle fibres of the Hill model can be evaluated analytically:

$$\begin{aligned} C_{ijkl}^{(\mathrm{f})} = {} & \bar{\lambda}/9(g'\bar{\lambda} + g)\delta_{ij}\delta_{kl} - \bar{\lambda}/3(g'\bar{\lambda} + g)(\hat{m}_i\hat{m}_j\delta_{kl} + \delta_{ij}\hat{m}_k\hat{m}_l) \\ & + \bar{\lambda}(g'\bar{\lambda} - g)\hat{m}_i\hat{m}_j\hat{m}_k\hat{m}_l + g\bar{\lambda}(\delta_{ik}\hat{m}_j\hat{n}_l + \hat{m}_i\delta_{jk}\hat{m}_l), \end{aligned} \tag{B8}$$

where $g' = \sigma_0(\partial f_{\mathrm{PEE}}/\partial\bar{\lambda}) + ((\kappa+1)/\kappa)\alpha\beta\mathrm{e}^{\alpha(\lambda_s - 1)}$ and $\kappa$ is a parameter relating the fibre stretch $\lambda$ with the corresponding stretches of the series elastic and the contractile element.

For the frog gastrocnemius muscle deformation problem (Subsection 3.2), the following Cauchy stress distribution

definition for the muscle connective tissues is adopted

$$\sigma_{ij}^{(\mathrm{ct})} = 2bc\mathrm{e}^{b(\bar{I}_1-3)}J^{-5/3}B_{ij} - [(2/(3J))bc\mathrm{e}^{b(\bar{I}_1-3)}\bar{I}_1 + 2K(1-J)]\delta_{ij}, \tag{B9}$$

where $b$, $c$ and $K$ are the material parameters, according to the work of Tang et al. (2007).

For this case, the material tangent stiffness tensor of Equation (B1) for the connective tissues is given analytically by the expression:

$$C_{ijkl}^{(\mathrm{ct})} = [4/(9J)(b\bar{I}_1+1)bc\mathrm{e}^{b(\bar{I}_1-3)}\bar{I}_1 + 2K(2J-1)]\delta_{ij}\delta_{kl} + 4b^2c\mathrm{e}^{b(\bar{I}_1-3)}J^{-7/3}B_{ij}B_{kl} + 2bc\mathrm{e}^{b(\bar{I}_1-3)}J^{-5/3}(\delta_{ik}B_{jl}+B_{il}\delta_{jk}) - 4/3(b\bar{I}_1+1)bc\mathrm{e}^{b(\bar{I}_1-3)}J^{-5/3}(B_{ij}\delta_{kl}+\delta_{ij}B_{kl}). \tag{B10}$$

Downloaded by [FORTH] at 05:27 28 July 2015